

## Article

# Property Variation of Extruded Mg-Gd Alloys by Mn Addition and Processing

Björn Wiese <sup>1,\*</sup> , Jochen Harmuth <sup>1</sup>, Regine Willumeit-Römer <sup>1</sup> and Jan Bohlen <sup>2</sup>

<sup>1</sup> Institute of Metallic Biomaterials, Helmholtz-Zentrum Hereon GmbH, 21502 Geesthacht, Germany; jochen.harmuth@gmail.com (J.H.); regine.willumeit@hereon.de (R.W.-R.)

<sup>2</sup> Institute of Material and Process Design, Helmholtz-Zentrum Hereon GmbH, 21502 Geesthacht, Germany; jan.bohlen@hereon.de

\* Correspondence: bjoern.wiese@hereon.de

**Abstract:** This paper presents how the mechanical properties, the microstructure and the degradation rate of extruded Mn-containing Mg-Gd alloys can be modified during extrusion. Gd as a rare earth element is particularly interesting due to the influence on the texture development in Mg, and is therefore studied as a base alloy system. The contents of Gd were investigated between 2 to 9 wt.%, with Mn additions of 0.5 and 1.0 wt.%. The grain sizes and the corresponding textures were modified by varying the extrusion parameters and the alloy content. It was shown that modification with Mn can lead to further grain refinement, an increase in the degree of recrystallization, as well as a decrease in the degradation rate in the biological medium compared with the binary Mg-Gd system from previous studies. The results suggest that the resulting properties are more robust compared with the binary alloy.

**Keywords:** Mg alloy; extrusion; rare earth elements; thermomechanical; processing; texture; degradable



**Citation:** Wiese, B.; Harmuth, J.; Willumeit-Römer, R.; Bohlen, J. Property Variation of Extruded Mg-Gd Alloys by Mn Addition and Processing. *Crystals* **2022**, *12*, 1036. <https://doi.org/10.3390/cryst12081036>

Academic Editor: Bolv Xiao

Received: 24 May 2022

Accepted: 20 July 2022

Published: 26 July 2022

**Publisher's Note:** MDPI stays neutral with regard to jurisdictional claims in published maps and institutional affiliations.



**Copyright:** © 2022 by the authors. Licensee MDPI, Basel, Switzerland. This article is an open access article distributed under the terms and conditions of the Creative Commons Attribution (CC BY) license (<https://creativecommons.org/licenses/by/4.0/>).

## 1. Introduction

Tailoring the properties of magnesium alloys is inevitable for their versatile application as a lightweight structural material or as a material for degradable implant applications. Pure magnesium itself features unfavourable properties such as unfavourable mechanical properties and corrosion resistance [1]. In particular, applying this material to implant applications requires adjusted alloying concepts to address the degradation or corrosion behaviour, and likewise to tailor mechanical properties, according to respective specifications. This is especially important if the material is subject to thermomechanical treatment carried out during forming, such as extrusion, which itself initiates a property profile development.

Rare earth elements (REE) are soluble in Mg alloys. In general, the addition of REE initiates weaker textures during processing which also improves the deformability [2–8]. Furthermore, high ductility at room temperature based on beneficial activation of more slip systems are also attributed to REE additions [4,5,8,9]. Recent developments have shown that alloying with gadolinium (Gd) maintains good biocompatibility of magnesium [10–15] as well as a potential to increase mechanical properties [8,16–20] and improve corrosion resistance [21,22].

In addition to Gd, manganese (Mn) has shown to be beneficial to the degradation behaviour of magnesium alloys as it is reducing the cathodic activity of impurities such as omnipresent Fe particles in the alloys [23–25]. Mn as an alloying element is mostly used in ternary Mg-Al-Mn alloys to form MnAl compounds that lead to higher corrosion resistance due to the reduced solubility for Fe [26] or by the formation of Al<sub>8</sub>Mn<sub>5</sub> phases that can substitute Fe into the Mn lattice sites [24,27]. The most beneficial ratio of Fe to Mn in Al-free Mg alloys is reported to be 0.036 or lower [24]. This also opens the possibility to tolerate higher Fe contents in Mg alloys when Mn is added in sufficient amounts. The addition of Mn to Mg-Gd shows increased corrosion resistance [28]. Compared to REE, the

addition of Mn to magnesium provides far less potential for solid solution strengthening. Only a limited maximum solubility of up to 2.2 wt.% is revealed (e.g., by thermodynamic calculations with Pandat<sup>TM</sup> 2017 and PanMagnesium 2017 database, CompuTherm, L.L.C., Middleton, WI, USA). As an example, the addition of 0.8 Mn to Mg–10Gd leads to finer grains after extrusion associated with  $\alpha$ -Mn precipitates which hinder recrystallization grain growth [29]. Extruded Mg–Mn alloys tend to form fibre-like textures with a special alignment of basal planes parallel to the extrusion direction if the extruded profile follows a round bar symmetry [7]. Such textures lead to limited ductility [5] and represent one reason why Mg–Mn alloys have not been considered for structural application despite excellent damping capacities [30] and good degradation properties [24]. Robson et al. [31] showed in early work that a suitable distribution of Mn particles could suppress recrystallization in binary Mg–Mn. However, Yu et al. [32] reported on as-extruded Mg–1Mn, whose features weakened texture and increased ductility due to coarse Mn precipitates present before extrusion.

In terms of biocompatibility, Mn serves as an essential trace metal in the human organism that is involved in several immune functions and aids in defence mechanics against free radicals [33]. The estimated safe and adequate dietary intake of is reported to be 2–5 mg/day for adults [34]. The tolerable upper intake level for adults based on a no-observed-adverse-effect level for Western diets was determined to be 11 mg/day [35]. Elemental Mn is also essential for bone growth as deficiencies may lead to bone resorption. Interestingly, non-experimentally induced Mn deficiency in humans has not been reported [33]. Contrary excess of Mn results in impaired bone development and neurotoxicity [36]. Such adverse health effects of Mn are primarily reported for inhaled Mn that will be transported directly to the brain before metabolization. An actual threshold level at which Mn exposure produces neurological effects in humans has not been established [35].

This work establishes a benchmark for Mg–Gd–Mn alloys in order to obtain a slow degradation behaviour and provide an array of mechanical properties that can be adjusted according to the specific requirements of applications. The approach is based on earlier work in Harmuth et al. [8] on binary extruded Mg–Gd alloys and addresses the impact of an addition of Mn in these alloys for the behaviour during extrusion and the resulting microstructural, mechanical and degradation properties.

## 2. Materials and Methods

The alloys were produced from pure magnesium (99.97%, Magnesium Elektron, Manchester, UK), pure Gd (99.90%, Dr. Ihme GmbH, Berlin, Germany) and Mg–2Mn (97.9 wt.% Mg with 2.08 wt.% Mn, Dead Sea Magnesium Ltd., Beer Sheva, Israel) as raw materials for casting. Permanent direct chill casting was conducted in a resistance furnace under protective atmosphere of argon with 3 vol.% sulphur hexafluoride (SF<sub>6</sub>). Pure magnesium and Mg–2Mn master alloy were molten at 720 °C followed by the addition of pure Gd. The melt was stirred at 250 rpm for 20 min and poured into preheated (650 °C) steel moulds with conical cylindrical dimension at a maximum diameter of 70 mm at the top and a total height of 230 mm. After placing the mould in a holding furnace at 650 °C for 2 min, it was slowly immersed into a water bath for a direct solidification of the ingot. The inner surface of the moulds is coated with boron nitride prior to pouring to allow for easy extraction after solidification. A list of all alloys investigated within this work is presented in Table 1. The scheme includes a variation of the Gd content in the range of 2 to 9 wt.% as well as an addition of 0.5 wt.% Mn or 1 wt.% Mn, respectively, thus remaining within a range of solid solubility for the respective sole alloying elements. The resulting chemical compositions of the alloys in the cast condition are shown in Table 1. The contents of Gd and Mn were measured by inductively-coupled plasma optical emission spectrometry. Values for Fe, Cu and Ni were determined by spark emission spectroscopy (ppm in weight). The ingots obtained were machined to cylinders of 49 mm in diameter and 150 mm length for the extrusion.

**Table 1.** Compositions with standard deviation of alloys in as cast condition. Contents of Gd and Mn were measured by inductively coupled plasma optical emission spectrometry, whereas levels of Fe, Cu and Ni were determined by spark emission spectroscopy.

Alloy	Gd [wt.%]	Mn [wt.%]	Fe [ppm]	Ni [ppm]	Cu [ppm]	Mg [wt.%]
Mg-2Gd-0.5Mn	2.27 ± 0.12	0.51 ± 0.02	24 ± 3	<13	<7	bal.
Mg-2Gd-1.0Mn	1.95 ± 0.06	0.94 ± 0.03	52 ± 3	<13	<7	bal.
Mg-4Gd-0.5Mn	4.18 ± 0.10	0.53 ± 0.03	56 ± 3	<13	<7	bal.
Mg-4Gd-1.0Mn	4.13 ± 0.12	0.95 ± 0.03	66 ± 3	<13	<7	bal.
Mg-9Gd-0.5Mn	9.01 ± 0.36	0.55 ± 0.02	58 ± 3	<13	<7	bal.
Mg-9Gd-1.0Mn	8.99 ± 0.14	1.06 ± 0.02	82 ± 3	<13	<7	bal.

After casting and machining, a heat treatment was conducted for all billets at 525 °C for 8 h under protective atmosphere with argon. Ingots were water-quenched immediately after heat treatment to ensure maximum solid solution. Furthermore, ingots were pre-heated to the respective extrusion temperatures for 1 h prior to extrusion in a furnace.

An automatic extrusion press (Müller Engineering GmbH & Co KG, Todtenweis, Germany) with a maximum force of 2.5 MN and a container with a diameter of 50 mm was used. Round bars with a diameter of 10 mm were produced with a flat die by applying indirect extrusion, corresponding to an extrusion ratio of 1:25. Extrusion parameter variations include two temperature settings (350 and 450 °C) and three ram speeds (0.6, 1.1 and 2.2 mm/s) for process parameter variation.

Microstructures of the extruded conditions were investigated throughout this work. Specimens were embedded in plastic cold-curing resin. Powdery and liquid Demotec 30 (Demotec Metallographie, Nidderau, Germany) were mixed in the weight ratio of 10:7. Microstructures of all materials investigated were obtained by grinding with silicon carbide papers of down to 2500 grit and polishing with 1 µm SiO<sub>2</sub> OPS (Oxide Polishing Suspension) (Cloeren Technology GmbH, Wegberg, Germany) with diamond 0.25 µm. Polished surfaces were cleaned using ethanol and dried under blowing hot air. Etching was conducted for about 10 to 15 s in a picric acid solution containing 20 mL distilled water, 200 mL ethanol, 7 mL glacial acetic acid and 15–20 g of picric acid followed by cleaning with ethanol and drying under blowing hot air.

Optical microscopy of the as-extruded samples was used to characterise microstructures with respect to the grain size and the fraction of recrystallized microstructure taken from an area analysis. Analyses were performed using a light optical microscope Leica DMI 5000 (Wetzlar, Germany). Grain sizes (GS) were determined on longitudinal sections (0.058 mm<sup>2</sup> each) by applying a line intersection method with grain boundaries as a mean value of three images per sample (top, middle, bottom).

Non-recrystallized fractions of the microstructure are more likely to be present in conditions of slow extrusion speeds and low temperatures due to retarded dynamic and/or static recrystallization. These areas can be easily identified by their elongated band-like structure with significantly larger dimensions compared to the surrounding recrystallized fine grains. The degree of recrystallization was analysed on longitudinal sections (5.8 mm<sup>2</sup> each) as a mean value of three images per sample (top, middle, bottom). These areas are quantified by computer aided area measurement and set in ratio to the full area investigated, thus labelled the fraction of recrystallized microstructure.

Scanning electron microscopy (SEM) was used to characterize particle morphologies. In addition, EDS was conducted to identify local compositions of specific areas and particles. Samples for SEM were prepared in identical fashion as for optical microscopy. However, no etching was conducted to guarantee an analysis of unaffected surfaces. SEM experiments were performed at an acceleration voltage of 15 keV and a working distance of 15 mm using a scanning electron microscope (TESCAN VEGA3-SB, Brno, Czech Republic) equipped with energy-dispersive X-ray spectroscopy (EDS) (IXRF Systems, IXRF, Austin, TX, USA).

The composition was recalculated with the software Iridium Ultra (IXRF, Austin, TX, USA) in wt.%.

Textures of all materials were measured in order to obtain information about grain orientations. Six pole figures were measured on polished cross sections of the extruded bars using X-ray diffraction and a goniometer setup (Malvern PANalytical, Kassel, Germany). Cu K $\alpha$  radiation with a beam size of 1.5 mm  $\times$  1 mm and tilt angles from 0° to 70° was applied. Texture evaluation is addressed by presenting inverse pole figures in the extrusion direction that are recalculated by using an open source code MTEX [37]. Due to the symmetry of the extruded cylindrical bars, the inverse pole figures in extrusion direction contain all relevant information to describe the texture.

Uniaxial tensile and compression testing was conducted at room temperature to characterize the mechanical properties of the extruded bars. Tensile test specimens were machined according to ISO 6892 Form B with a diameter of 5 mm and a gauge length of 25 mm. Compression test specimens were machined to a diameter of 8 mm and a length of 12 mm. All tests were performed using a universal testing machine Zwick Z050 (ZwickRoell GmbH & Co. KG, Ulm, Germany) at room temperature and at a constant initial strain rate of 10<sup>-3</sup> s<sup>-1</sup>. An evaluation of the hardness was conducted using an EmcoTest M1C 010 (Salzburg, Austria) machine based on ISO 6507-1 by using the software EmcoTest M41Eht v4.20.8.0 of the company Osterer (Jacksonville, FL, USA). Vickers hardness was determined with a load of 5 kg and a dwell time of 30 s. On average, 12 measurements were taken for each sample.

Degradation properties of all alloys were evaluated by weight loss measurement of 3 samples after 7 days in a semi static immersion test. All tests were conducted under cell culture conditions (37 °C, 5% CO<sub>2</sub>, 20% O<sub>2</sub>, 95% relative humidity) in Dulbecco's modified eagle medium + Glutamax (DMEM, Fisher Scientific, Schwerte, Germany) + 10% fetal bovine serum (FBS, PAA Laboratories, Cölbe, Germany). The composition of DMEM consists of 6 salts and glucose supplemented by 13 essential amino acids and 8 vitamins. The medium was changed every two days with simultaneous measurement of pH and osmolality.

Prior to immersion, samples were ground with 2500 SiC paper, cleaned for 20 min in hexane, 20 min in acetone, 5 min 100% ethanol all in ultrasonic bath (Merck KGaA) and sterilised for 5 min in 70% ethanol, following established laboratory routine. Final sample dimensions after grinding were 1.4 mm height and 9 mm diameter. After immersion, corrosion products were removed by immersion in chromic acid (180 g/L in distilled water, Sigma-Aldrich) for 20 min. The weight after removal of corrosion products was measured. The degradation rate (DR) [mm/year] was determined by applying Equation (1) with  $\Delta m$ —weight change after immersion,  $A$ —surface area,  $t$ —immersion time and  $\rho$ —density. Density was determined following Archimedes principle using a scale (Sartorius LA 230 S, Burladingen, Germany) with setup for density measurements by buoyancy method in ethanol.

$$DR = \frac{\Delta m}{A \times t \times \rho} \quad (1)$$

### 3. Results

#### 3.1. Extrusion Forces

The extrusion experiment is characterized by a force increase to a peak level during the initiation of the material flow and a constant steady state force level during processing. The reader is referred to earlier work for the visualization of such a diagram which only varies in the reached levels of forces for the materials in this study [38]. Both forces increase as the speed increases, or the extrusion temperature decreases (Figure 1). This refers to lower flow stresses with increasing temperature where also increased deformation related heating with higher speed will be the dominating effect. At lower temperatures, the increasing Gd content leads to a distinct increase in forces, whereas the influence of the Mn content is negligible. At 350 °C, the forces increase more significantly with higher Mn content than

during extrusion at 450 °C. In particular, the difference in peak forces is more pronounced for the alloys with the higher Mn content at 350 °C. An increase in speed has a marginal effect on the forces only.

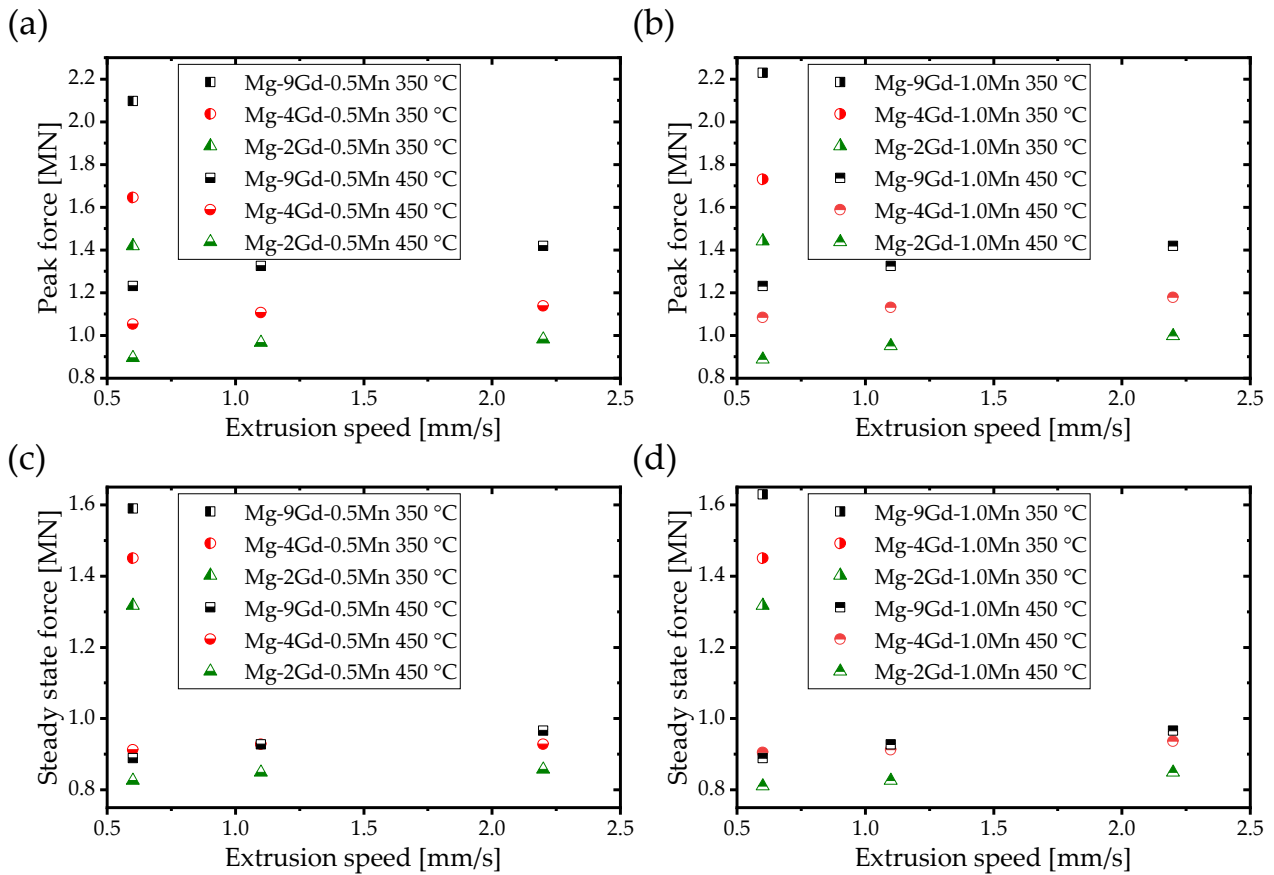


**Figure 1.** Extrusion forces peak force for Mg-xGd-0.5Mn (a) and for Mg-xGd-1.0Mn (b) and steady state force for Mg-xGd-0.5Mn (c) and for Mg-xGd-1.0Mn (d) with respect to extrusion parameters.

### 3.2. Microstructure

The effect of Mn addition and the process parameters on the microstructure is demonstrated in Figures 2 and 3, using two sets of results as exemplary examples. Figure 2 shows the influence of the Gd content (from left to right) on the microstructure development and the impact of increased Mn content (from top to bottom). Higher Gd content leads to an enhanced degree of the recrystallized microstructure at these lowest speed and temperature settings as well as visible grain growth. The influence of Mn, i.e., a change from 0.5 wt.% Mn to 1.0 wt.% leads to a stabilization of the grain size development even at higher Gd content. This stabilization persists if the extrusion temperature is increased, Figure 3a,b, still revealing coarser-grained microstructures if compared to Figure 2. An increase in the extrusion speed exhibits a similar effect. The influence of both extrusion parameters, temperature and extrusion speed on the grain size and the fraction of recrystallized microstructure is collected in Figure 4. Generally, an increase in extrusion speed and temperature results in an increased fraction of recrystallized microstructure and an increase in the grain size.

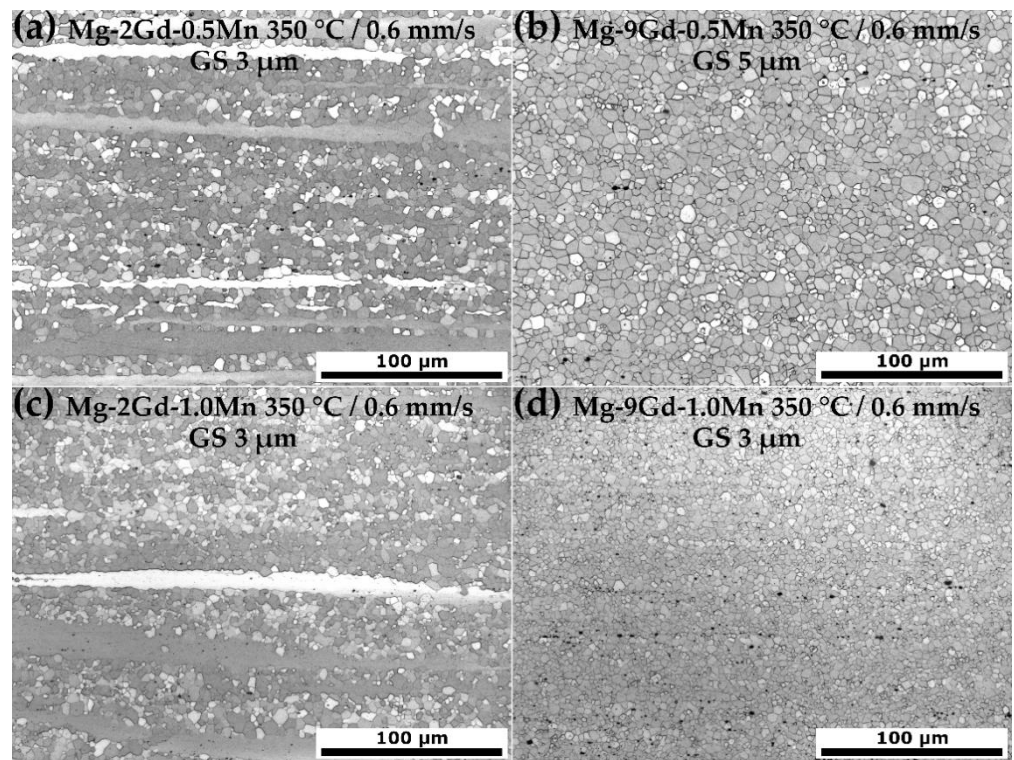


**Figure 2.** Light optical micrographs with average grain size (GS) of Mg-2Gd and Mg-9Gd with 0.5 and 1.0 wt.% Mn with respect to extrusion temperature (extrusion direction horizontal).

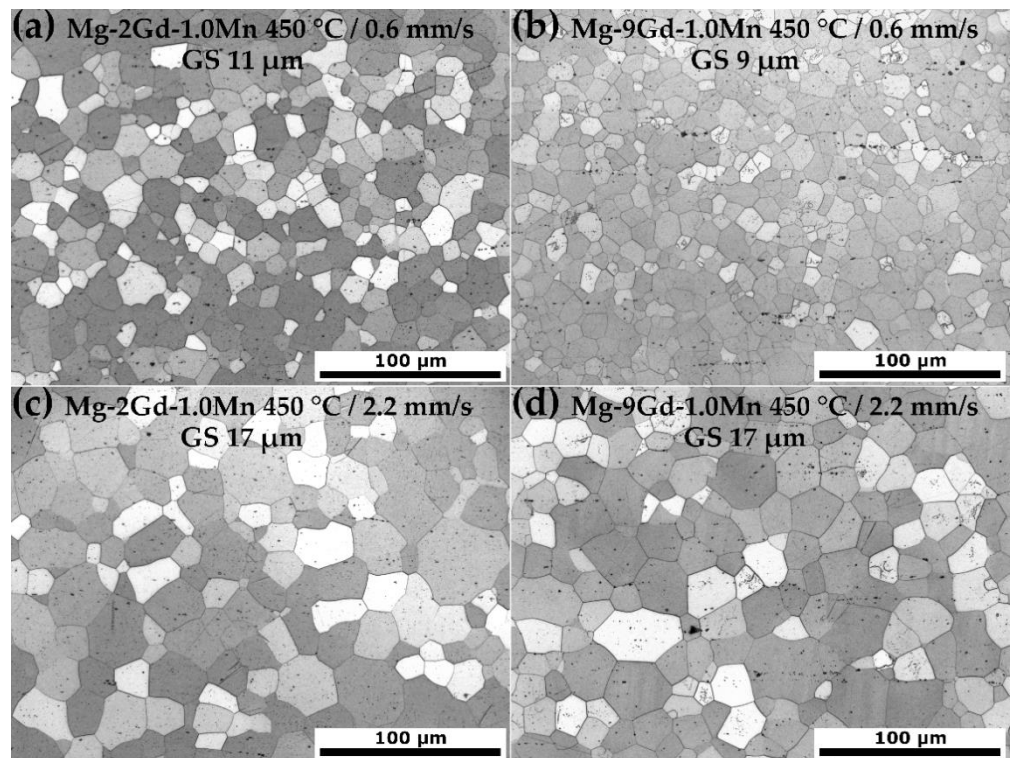


**Figure 3.** Light optical micrographs with average grain size (GS) of Mg-xGd-1Mn (x = 2 and 9 wt.%) with respect to extrusion speed (extrusion direction horizontal).

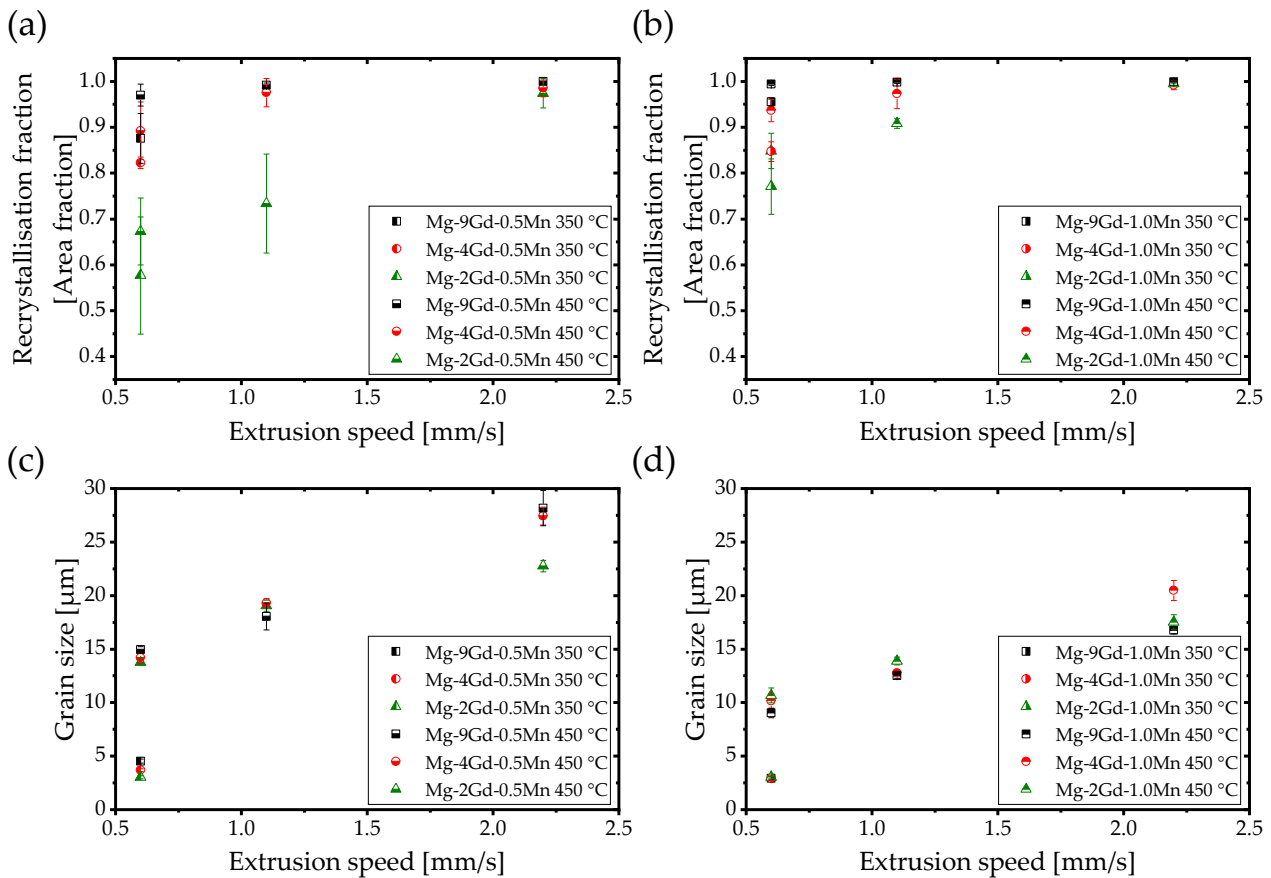


**Figure 4.** Degree of recrystallization for Mg-xGd-0.5Mn (a) and for Mg-xGd-1.0Mn (b) and grain size with respect to extrusion parameters for Mg-xGd-0.5Mn (c) and for Mg-xGd-1.0Mn (d). Error bars are standard deviations.

For Mg-xGd-1Mn the overall degrees of recrystallization are at high levels (Figure 4a,b). The slowest speed of 0.6 mm/s is accompanied by not fully recrystallized microstructures in Mg-2Gd-1Mn and Mg-4Gd-1Mn. However, in Mg-9Gd-xMn it can be considered fully recrystallized (Figure 2b,d). Compared with Mg-xGd-0.5Mn, the addition of 1Mn significantly increases the degree of recrystallization. Results reveal a homogeneous distribution of equiaxed fine grains for all alloys in all conditions with partially recrystallized areas present for lower extrusion speed and temperature (Figures 2 and 3). Both concentrations of Mn in the system show a similar influence of extrusion parameters on the grain sizes. Grain sizes are gradually increased with increasing extrusion speeds and temperatures. However, a difference between the addition of 0.5 Mn or 1 Mn becomes visible in the grain sizes (Figure 4). The grain sizes of Mg-Gd-0.5Mn and Mg-Gd-1Mn are visualized in Figure 4c,d. For Mg-Gd-0.5Mn grain sizes range from 3 to 28 μm. Contrary, for Mg-Gd-1Mn grain sizes range from 3 to 21 μm revealing a decrease in grain size for extrusions at 450 °C. Secondary particles are present in all the microstructures.

The effect of the process parameters on the texture development of Mg-xGd-yMn is shown in the Figure 5 using the example of the Mg-xGd-1.0Mn series. An influence of the Mn content is negligible and shows a similar texture, with the maximum intensity tending to be slightly lower with increasing Mn content. The maximum intensity decreased with increasing Gd content and extrusion speed. Increasing the temperature at low extrusion speed first maintains the significance of a  $\langle 1100 \rangle$  pole prismatic fiber component, which is associated with the unrecrystallized fraction of the microstructure. This significance decreases with increasing speed but also with increasing content of Gd.

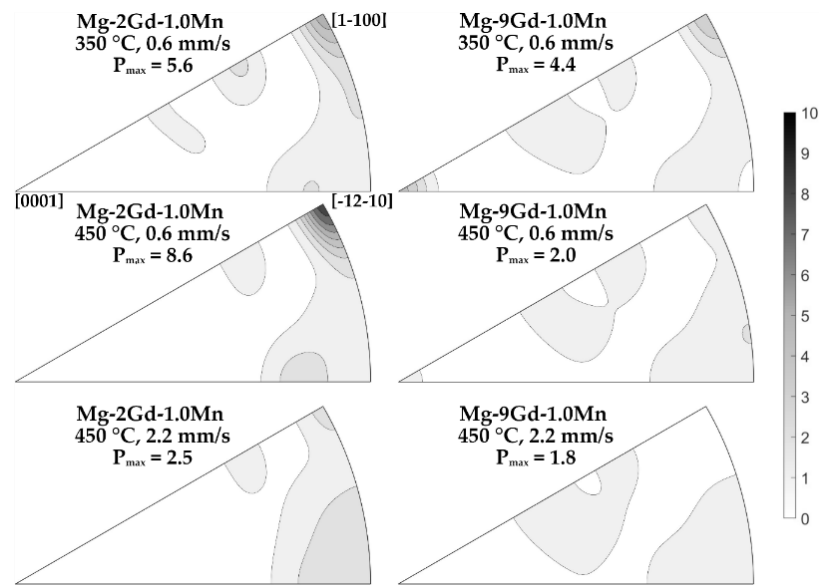


**Figure 5.** Inverse pole figures in ED of as extruded Mg-xGd-1Mn with respect to extrusion parameters. Bottom left [0001] pole, bottom right  $[\bar{1}2\bar{1}0]$  pole and top right  $[1\bar{1}00]$  pole with intensities ranging from 0 to 10.

Intensities at the [0001] pole are visible at high Gd content and lower thermal impact but vanish with increasing extrusion speed. No intensities at the [0001] pole are present in Mg-2Gd-yMn. With increasing Gd content in the alloys and with increasing extrusion speed, the intensities decrease and shift from the  $\langle 1\bar{1}00 \rangle$ -to  $\langle \bar{1}2\bar{1}0 \rangle$ -poles. At high speed and temperature, very weak textures are obtained with almost random character while maintaining a preferential orientation range around the  $[\bar{1}2\bar{1}0]$  pole, as well as a tilt component of basal planes out of the extrusion direction.

Exemplary EDS analysis was conducted on Mg-9Gd-1.0Mn with the highest proportion of second phases. Results are shown in Figure 6. The particles are not preferentially located at the grain boundaries but are lined up as stringers in the extrusion direction, therefore indicating their existence even prior to extrusion. Two types of second phases can be distinguished, a Gd-rich (up to 100 wt.% Gd) and a Mn-rich (up to 95 wt.% Mn). A Gd content in the Mn-rich particles most likely results from a small overlap of the Gd and Mn EDS spectra (Mn:  $K\alpha 1$  and  $K\alpha 2$  at 5.89 kV and Gd:  $K\alpha 1$  and  $K\alpha 2$  at 6.05 kV). The Gd-rich particles are of rectangular shape with a size of up to 3  $\mu\text{m}$  Figure 6b in all alloys and under all conditions. This kind of morphology has been associated with  $\text{GdH}_2$  in other works [39–45]. Although the hydrogen content cannot be revealed by the applied method, it is easily hypothesized that the high Gd-containing particles are of this nature. The amount of these particles increases with the Gd content. However, the Mn-rich particles have a round shape with a diameter of less than 1  $\mu\text{m}$ , Figure 6c, and can only be observed in the Mg-xGd-1.0Mn series with higher Mn-content. In context to the above-mentioned thermodynamic calculations where the applied heat treatment allows assuming full solid solution of the alloying elements, it can be concluded that the dissolution of Mn in this alloy is not fully reached in the higher Mn-containing alloys, whereas the expected full dissolution of Gd may be hindered due to the formation of hydrides. It is not expected that this deviation from solid solution alone will explain the underlying impact of the alloying elements on the microstructure and the mechanical properties.

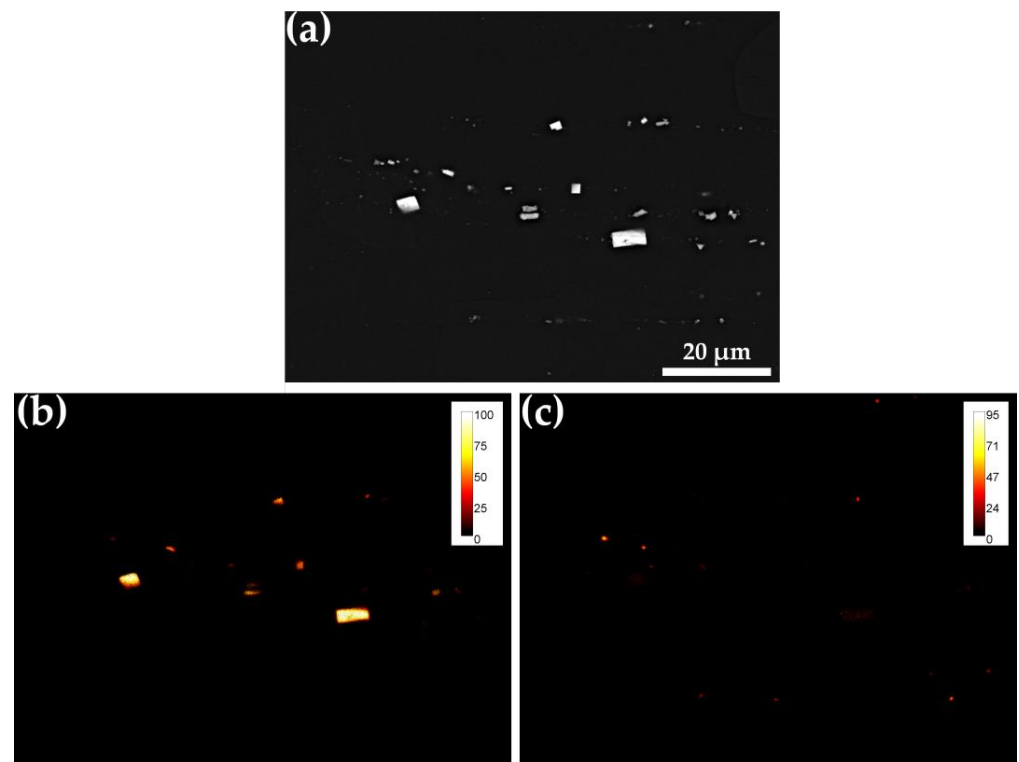


**Figure 6.** Mg-9Gd-1Mn extruded at 450 °C/2.2 mm/s in (a) SE mode with (b) Gd and (c) Mn element maps in wt.%. Gd-rich with distinct rectangular shape present and small Mn-rich particles (pure Mn).

### 3.3. Mechanical Properties

The mechanical properties in tension and compression are collected in Table 2. A small increase in the yield strength and the ultimate stress with higher Mn content is more pronounced at higher Gd content. Generally, the thermal impact (with higher extrusion temperature or higher extrusion speed) leads to a reduction in strength values concurrent to the above-mentioned grain coarsening. The same tendency is found for the hardness, which is mainly influenced by the temperature and the Mn content in the alloy series. An increase in extrusion speed shows a more pronounced decrease in yield strength, ultimate strength and hardness at higher Gd contents, but with a higher Mn content, the values increase at identical Gd content.

While there is an increase in the elongation to fracture ( $\epsilon_t$ ) along tension at higher extrusion temperature only and with increasing Mn content, this effect is not distinct with higher content of Gd where a general increase due to the addition of Gd is already noticed. In contrast to this, compression to fracture ( $\epsilon_c$ ) achieves the lower values at the lowest extrusion temperature and lowest Gd content.  $\epsilon_c$  is mainly not changed with Mn content.

The changes in the stress–strain curves are shown for the examples with the lowest and highest Gd concentrations with 1.0 wt.% Mn at 350 °C and 450 °C at 0.6 mm/s in Figure 7. Note that changing the extrusion speed also changes the mechanical properties from tensile and compression test, but not the characteristic shape of the stress–strain curves itself. These results for the tensile test show a clear yield stress for Mg-2Gd-yMn, which transitions to the yield point at higher Gd content. At 350 °C this yield stress is still present, but at 450 °C a yield point is almost reached for the Mg-2Gd-yMn alloys. In the compression test, the S shape is present at both temperatures for the Mg-2Gd-yMn and Mg-4Gd-yMn materials. This S shape disappears with the highest Gd concentration and can no longer be determined for the Mg-9Gd-yMn. While this describes a sole effect of the Gd-content, the Mn content does not exhibit a distinct influence on the shape of the flow curves. A similar trend is revealed if the asymmetry of the flow behavior in the form of the difference between TYS and CYS is assessed, see also Table 2 as the CYS/TYS ratio. A

higher content of Gd leads to an increase in this ratio, which is accompanied by a change in the shape of the stress–strain curves. Again, the Mn content does not add a distinct change.

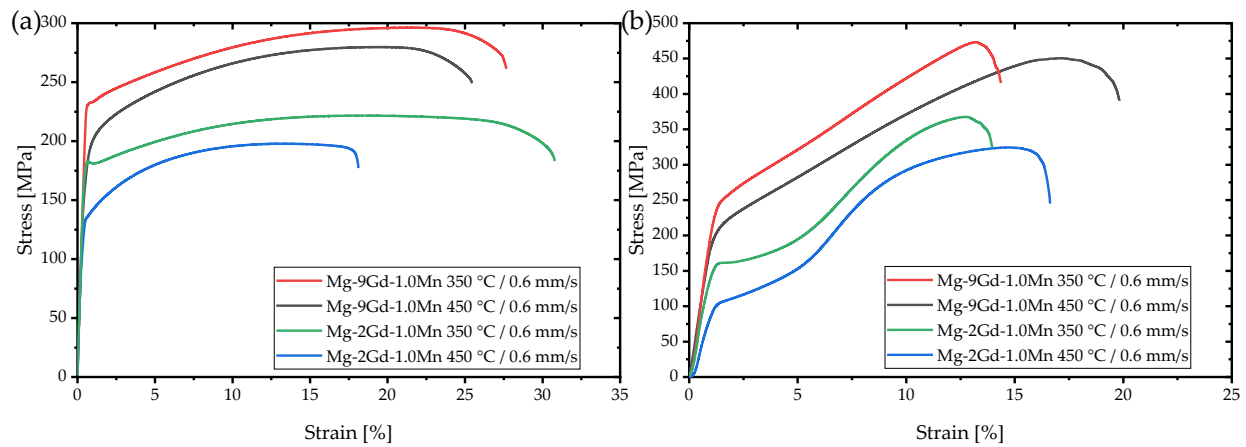


Figure 7. Examples of the stress–strain-curves from (a) tensile and (b) compression test.

Table 2. Mechanical properties with respect to extrusion parameters and alloy.

Alloy	T [°C]	Ext. Speed [mm/s]	TYS [MPa]	UTS [MPa]	$\epsilon_t$ [%]	CYS [MPa]	UCS [MPa]	$\epsilon_c$ [%]	CYS/TYS	Hardness [HV]
Mg-2Gd-0.5Mn	350	0.6	184 ± 1	217 ± 1	31.5 ± 1.1	157 ± 1	360 ± 7	12.8 ± 1.3	0.85	59.6 ± 1.4
		0.6	137 ± 3	187 ± 1	9.9 ± 2.3	94 ± 2	309 ± 4	13.7 ± 1.0	0.69	45.3 ± 1.0
		1.1	116 ± 4	185 ± 1	16.8 ± 4.4	76 ± 8	310 ± 6	19.7 ± 2.7	0.66	45.3 ± 1.1
Mg-2Gd-1.0Mn	450	2.2	104 ± 1	181 ± 1	22.0 ± 2.2	86 ± 4	330 ± 6	25.5 ± 1.2	0.83	43.4 ± 1.1
		0.6	184 ± 1	222 ± 1	30.8 ± 1.2	155 ± 2	367 ± 1	12.6 ± 0.4	0.84	58.9 ± 1.1
		0.6	128 ± 2	197 ± 1	18.4 ± 1.5	99 ± 1	324 ± 2	14.8 ± 1.1	0.77	48.8 ± 1.7
Mg-2Gd-1.0Mn	450	1.1	120 ± 2	194 ± 1	20.8 ± 1.8	79 ± 7	320 ± 2	17.5 ± 0.6	0.66	45.5 ± 1.1
		2.2	105 ± 2	189 ± 1	27.6 ± 1.6	81 ± 8	315 ± 4	19.1 ± 0.9	0.77	44.6 ± 0.9
		0.6	173 ± 2	225 ± 1	26.2 ± 1.9	163 ± 3	368 ± 7	16.4 ± 0.7	0.94	64.3 ± 0.9
Mg-4Gd-0.5Mn	350	0.6	134 ± 3	206 ± 2	16.5 ± 1.2	108 ± 11	347 ± 5	20.3 ± 1.4	0.81	53.2 ± 1.4
		1.1	114 ± 3	200 ± 1	25.1 ± 1.8	117 ± 3	357 ± 6	24.5 ± 1.5	1.03	52.0 ± 0.8
		2.2	109 ± 2	198 ± 1	26.7 ± 1.0	116 ± 1	355 ± 5	24.5 ± 0.9	1.06	50.5 ± 1.1
Mg-4Gd-1.0Mn	350	0.6	187 ± 2	238 ± 1	25.8 ± 0.6	169 ± 4	382 ± 3	16.0 ± 0.7	0.90	67.8 ± 1.6
		0.6	143 ± 2	220 ± 1	21.6 ± 1.1	142 ± 1	365 ± 2	20.9 ± 0.9	0.99	58.0 ± 0.9
		1.1	135 ± 3	216 ± 1	23.2 ± 2.0	132 ± 8	363 ± 4	22.1 ± 1.3	0.98	56.3 ± 0.6
Mg-4Gd-1.0Mn	450	2.2	115 ± 2	206 ± 1	27.9 ± 2.1	123 ± 7	374 ± 2	25.7 ± 0.5	1.07	54.3 ± 1.3
		0.6	212 ± 1	287 ± 1	26.6 ± 0.5	227 ± 4	458 ± 2	12.5 ± 0.4	1.07	86.2 ± 1.2
		0.6	164 ± 2	268 ± 1	22.9 ± 1.7	184 ± 6	430 ± 3	19.3 ± 0.6	1.12	75.8 ± 0.9
Mg-9Gd-0.5Mn	450	1.1	145 ± 3	257 ± 2	24.4 ± 0.6	194 ± 2	420 ± 3	18.5 ± 0.1	1.34	74.6 ± 1.8
		2.2	138 ± 6	248 ± 1	25.0 ± 1.5	186 ± 2	418 ± 3	19.0 ± 0.5	1.35	74.7 ± 1.8
		0.6	233 ± 1	297 ± 2	26.9 ± 0.4	253 ± 2	475 ± 4	12.4 ± 0.3	1.09	90.8 ± 0.7
Mg-9Gd-1.0Mn	350	0.6	183 ± 4	281 ± 1	24.2 ± 3.1	206 ± 4	452 ± 2	18.1 ± 0.4	1.13	81.4 ± 0.8
		1.1	166 ± 7	271 ± 1	24.8 ± 0.3	191 ± 10	440 ± 3	19.0 ± 0.3	1.15	79.5 ± 1.3
		2.2	154 ± 7	262 ± 1	26.0 ± 0.7	187 ± 3	432 ± 1	19.3 ± 0.5	1.21	77.5 ± 0.9

### 3.4. Degradation

Generally, low DRs, e.g., lower than 0.3 mm/year, are determined for all materials in all conditions as visualized in Figure 8. Additionally, for all alloys, results of initial degradation testing are not affected by the extrusion parameters. No statistically significant difference is detected within the conditions of each single alloy or between all alloys. However, there is a trend visible where higher additions of Gd lead to slightly lower DRs.

On the contrary, an expected impact of the Mn concentration, i.e., lower DR at higher Mn content, is only found for the lowest Gd-containing alloys. The addition of 1 wt.% Mn leads to an average DRs of 0.27 mm/year to 0.18 mm/year in Mg-2Gd-yMn and 0.13 mm/year to 0.19 mm/year in Mg-4Gd-yMn. Thereby, the DR decreases for 2Gd-1.0Mn and slightly increases for Mg-4Gd-1.0Mn. The average DRs for Mg-9Gd-xMn are increased from 0.08 mm/year to 0.12 mm/year with more Gd.

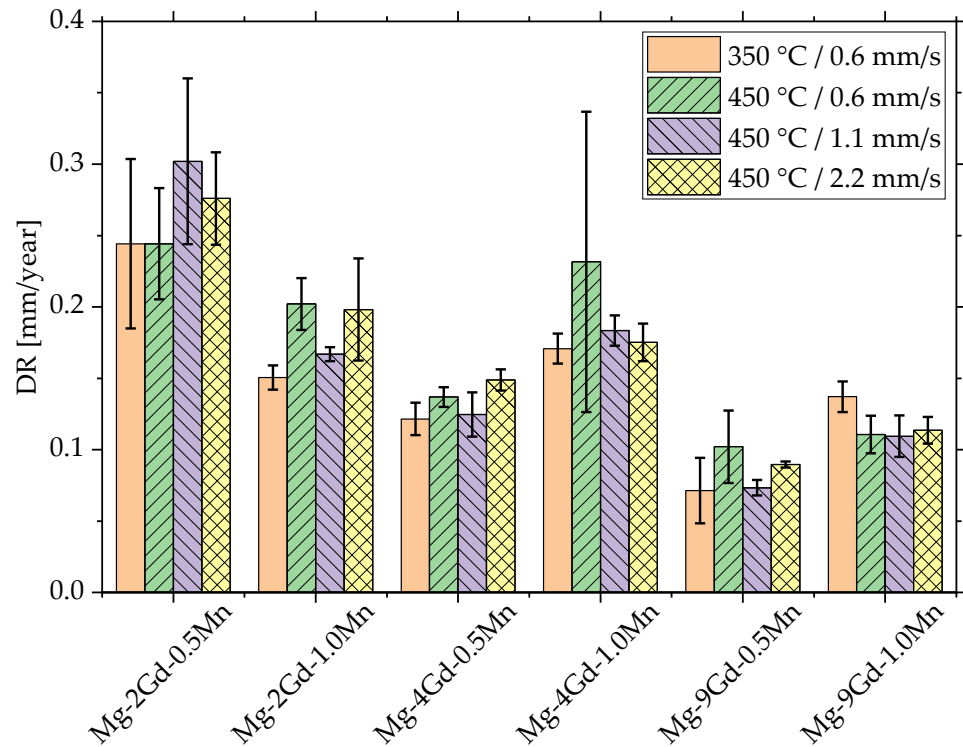


**Figure 8.** Degradation rates (DR) based on weight loss after 7 d immersion for Mg-Gd-0.5Mn Mg-Gd-1.0Mn. Values for Mg-Gd are shown as reference. Error bars are standard deviation. Degradation rates of Mg-Gd are shown as reference. Error bars are standard deviations.

#### 4. Discussion

During indirect extrusion the applied force increases to an initial peak value when the material flow starts and then decreases to a steady-state level during continuous material flow. A direct correlation between the speed of the extrusion ram and the force can be attributed to the influence of the alloying elements in solid solution during the extrusion process (Figure 1). In the case of this study, the increasing Mn content shows a negligible influence on the force increase at 450 °C, but a visible increase at 350 °C. While precipitates are visible and a visible amount of Mn particles is identified, especially at higher Mn content, solid solution strengthening is a consistent explanation for the increased forces with increasing Mn content, as well as with the Gd content. At higher temperatures, Gd and Mn are less effective as enhancers of strength because atoms and dislocations are more mobile during massive deformation of the crystals. At the same time, the higher temperature allows activation of additional slip systems and promotes softening processes such as dynamic recrystallisation [39]. The equilibrium force is lower than the peak force, which is due to the introduction of the deformation heat during the process. The dependence of the forces on the deformation rate can be related to the increasing extrusion speed and the respective yield stress of the materials and parameters.

Increasing deformation-related heating, i.e., temperature, as well as extrusion temperature leads to changes in the grain structure, as the higher temperatures lead to increased diffusion rates [39]. This can lead to increased recrystallization resulting in a larger grain

size as well as a corresponding change in texture. The effects on recrystallization and grain size can be confirmed by the results obtained in Figure 4. The addition of 0.5 wt.% Mn has no effect on grain size and degree of recrystallization in the Mg-Gd system [20]. For Mg-xGd-0.5Mn, the grain size is in a similar range from 3  $\mu\text{m}$  to 28  $\mu\text{m}$  (Figure 4c), as in the binary Mg-Gd system from the extrusion study [20] from 3  $\mu\text{m}$  to 25  $\mu\text{m}$ . The effect of 1 wt.% Mn addition in the present work results in a reduction in the grain size from 3  $\mu\text{m}$  to 20  $\mu\text{m}$  (Figures 3 and 4d). Thus, at higher extrusion speeds, the Mn somewhat retards grain growth (higher deformation-induced heating) and does not act as a recrystallization grain nucleus. This can be concluded from the comparable grain size at lower extrusion speeds between both Mn content alloys. A similar conclusion was drawn by Robson et al. [31], who reported that Mn particles of appropriate size and distribution preserve the grain structure after rolling and heat treatment. Mn reduces grain growth but increases the amount of recrystallized areas at lower temperature and low extrusion speeds (Figures 2 and 4a,b). Growth restriction was also proved in extruded Mg-10Gd with 0.9 wt.% Mn [29] and Mg-1Gd-Mn alloys [40] by pinning the grain boundaries, as well for as extruded Mg-1Mn [32]. Gd also increases the resulting degree of recrystallization while not increasing the grain size at higher Gd contents, even in the binary system. In the case of Gd, this can be attributed to the effect of solute segregation to the grain boundaries and solute drag, as suggested by Robson et al. [41] and in agreement with the findings of Harmuth et al. [20].

As mentioned above, Mn precipitation occurs at higher Mn contents, as shown in Figure 6. This is in good agreement with the low solubility of Mn in Mg. These Mn particles appear to reduce grain growth, as mentioned earlier. The amount of Gd-rich particles increases with Gd content, but has no effect on grain size, as has been reported for the binary Mg-Gd system [20]. Rectangular precipitates with this high Gd content are the RE hydrides [42,43] of Gd, i.e.,  $\text{GdH}_2$  [44,45].

Main and similar effect on the texture can be attributed to the Gd content in a binary system as discussed in Harmuth et al. [20] with the formation of the “rare earth” texture [40]. However, an increase in the Gd content and speed also increases the fraction of recrystallized microstructure and reduces the significance of the texture. The orientation of basal planes perpendicular the [0001] pole to the extrusion direction is present for higher Gd contents and vanished with higher extrusion speed and temperature. An proposed explanation is given from Harmuth et al. [20] based on a combination of shear band recrystallization, the solute drag effect and a non-basal slip activation [46,47]. The effect of addition of Mn alone is hardly visible. This is due to the prominent effect of Gd on the corresponding textures. The texture changes because of the activation of deformation mechanisms such as slip and twinning [8,20,47,48]. As a comparison, textures of as-extruded Mg-1Mn addition have been reported by Bohlen et al. [7]. At slow extrusion, textures in Mg-1Mn possess a fibre-type texture with intensities distributed on the arc between the  $\langle 1\bar{1}00 \rangle$ - and  $\langle \bar{1}2\bar{1}0 \rangle$ -poles. This corresponds well with the general textures in the Mg-Gd-Mn alloys of this work. Bohlen et al. [7] also reported that an increase in the extrusion speed leads to intensities shifted towards the  $\langle \bar{1}2\bar{1}0 \rangle$ -pole and a weakening of the texture. Similar results are obtained from ME11 alloy (1 wt.% Mn, 1 wt.% Ce) but with slightly increased maximum intensities for slow extrusions. Overall, the textures in this work are slightly weakened when Mn is added to binary Mg-Gd. This is contradictory to the findings of Yu et al. [31] reporting on stronger texture in as-extruded binary Mg-1Mn alloys compared with pure Mg.

The strengthening can be referred to a solid solution strengthening by alloying additions as well as concurrent grain refining. The solid solution strengthening is also confirmed by the extrusion forces values at the elevated process temperatures. Compared with the binary Mg-Gd material described by Harmuth et al. [20], the yield strength is at similar levels, as shown in Figure 9. Thereby the CYS levels fit well with the grain size dominated flow consideration (Hall–Petch relation) of the binary Mg-Gd system. However, the TYS values are at higher stress levels compared to a data fit of the binary alloys taken from Harmuth et al. [20]. This can indicate that Mn has an anisotropic effect on the strengthening

in relation to the load direction. It is also evident for alloys that the slopes for TYS are not identical if the binary alloys from the earlier work and the Mn-modified alloys from this study are compared. One reason for this could be attributed to the incompletely recrystallized microstructure at lower temperatures and speeds of the binary material and a higher degree of recrystallization with the addition of Mn. Furthermore, the texture is most pronounced in these states, so that the impact of basal slip on this strength value is reduced (due to the unfavorable alignment and corresponding lower Schmid factors). Evidence for this is the yield point in the tensile tests on these materials, as exemplarily shown in Figure 7a. With higher Gd and Mn content, the UTS and UCT are significantly higher than for the binary Mg-10Gd in Harmuth et al. [20] compared with the Mg-9Gd-yMn and in a similar range for Mg-4Gd-yMn compared to Mg-5Gd [20]. This shows that the Mn additions can substitute Gd in this system as solid solution strengthener in slip-dominated flow while not in twin dominated flow as seen in the CYS in Figure 9a. In the same time Mn is also reducing the grain size with 1 wt.% Mn. The hardness of the different materials follows an identical trend as the yield strengths and ultimate strengths, reflecting the strengthening due to solid solution strengthening and grain boundary strengthening.

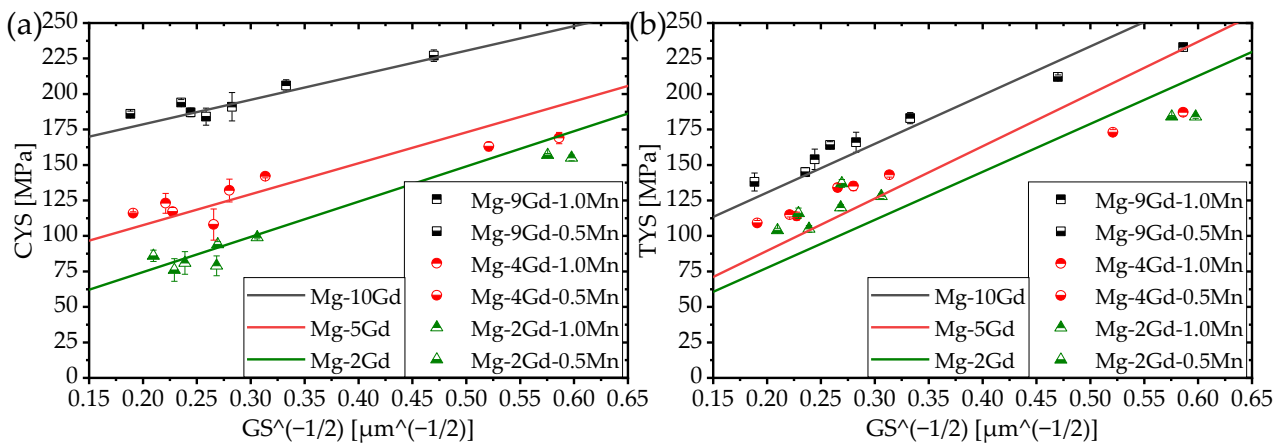


**Figure 9.** Hall-Petch relation for (a) CYS and (b) TYS from this work compared to the Hall-Petch fit for Mg-2Gd, Mg-5Gd and Mg-10Gd from Harmuth et al. [8].

The crystallographic orientation with respect to the loading direction and the alloy composition in the hcp metals will influence the yield strength. For pure Mg, a tensile-compression yield strength asymmetry of  $CYS/TYS < 1$  is obtained in the extruded material. Anisotropy in comparison between tension and compression deformation can be seen in Figures 7 and 9 and Table 2. This asymmetry is reversed with increasing Gd content and finer grains, as shown in Table 2 as the CYS/TYS ratio. Some studies [8,16,20] suggested that reverse flow asymmetry is caused by changes in the twin-related deformation. With increasing Gd content, the  $[101\bar{2}]$  twinning is increasingly inhibited by the short-range order. With increased Gd content in the solid solution, on the other hand, the  $[101\bar{1}]$  compression twinning is still active [8,16,20]. This explains the difference in the stress-strain curve in the compression test. With low contents of Gd, an S-shaped curve can be determined after exceeding the yield stress, but not with higher contents of Gd. This inflection point in the S-shaped curve corresponds to a change in the deformation process during the test; according to the work of Dobroń et al. [49], this can be explained by an initial hardening due to the growth of the tensile twins followed by dislocation slip of the material. However, the clear difference in the curves of Mg-10Gd supports the theory that twinning is active during compression with low Gd contents, but suppressed during compression with higher Gd contents. There is no significant difference between this behavior and that of the binary Mg-Gd system due to the addition of Mn [8,16,20].

The degradation rate is low and appears suitable for biomedical applications, and is likewise in the binary Mg-Gd system [20]. Moreover, the DR is independent of the processing parameters, grain sizes or microstructural features. There is also a visible trend, namely, that more Gd reduces the DR in the material with 0.5 wt.% Mn, and with 1 wt.% Mn the DR are all at the same level. In the previous study, the values for Mg-10Gd [20] result in an average DR of 0.16 mm/year compared with Mg-9Gd-0.5Mn with an average DR of 0.08 mm/year, implying a reduction in DR at high Gd contents. For the lower Mg-2Gd and Mg-5Gd [20], i.e., the lower Gd contents, average DRs of 0.24 mm/year and 0.21 mm/year were achieved. These values are in the range of the values determined in this work with low Gd contents. However, higher Gd and Mn content are also associated with a higher Fe contamination (Table 1); thus, the sources of this contamination are the alloy additions themselves. This is surprising, as Fe has a negative effect on the corrosion or degradation resistance, which cannot be confirmed at this point. Harmuth et al. [20] already reported that the higher Fe content in the binary Mg-Gd system caused no problem regarding the DR under in vitro conditions. The present work can confirm this conclusion on the effect of Gd and Fe contamination. However, the DR is also at a lower level with similar Fe contamination, except for the Mg-2Gd-0.5Mn series. At the same time, the DR with 1 wt.% Mn is slightly higher than the low DR results with 0.5 wt.% Mn. This might be related to a higher fraction of Mn particles and more Fe, leading to a higher DR. On the other hand, Mn is known to be beneficial for increasing corrosion or degradation resistance in some systems [23–28]. According to Campos et al. [28], the addition of Mn to cast Mg-10Gd in NaCl solution enhances the formation of the passive layer on the surface and thus may improve corrosion or degradation resistance. A protective passivation layer can even lower the DR with more Fe. This seems to provide a robust combination for this degradation resistance in the ternary system with increased Mn content. The interaction of Gd and Mn content in Mg alloys on the degradation behaviour should therefore be addressed in further studies.

## 5. Conclusions

The recrystallization of the REE (Rare earth elements)-containing Gd-based Mg alloy can be improved by varying the extrusion process parameters and the Mn additions. This allows an adjustment of the property profile in a similar range with higher strengths at the same grain sizes compared to the binary Mg-Gd system [20]. Adjustment of mechanical properties in the range between TYS 104–233 MPa, UTS 189–297 MPa, elongation at fracture 9.9–31.5%, CYS 76–253 MPa, UCS 309–475 MPa, fracture pressure 12.4–25.7 MPa and hardness 43.4–90.8 HV is possible. Increasing the Mn content from 0.5 to 1.0 wt.% reduces grain growth by suppressing grain boundary movement by Mn particles, which has been mentioned in other studies on Mg-Mn systems. The Gd and Mn content leads to improved recrystallization without grain growth in the material, which allows processing at lower temperatures. The strengthening can be attributed to solid solution strengthening and grain refinement. The asymmetry of the tensile-compressive yield strength reverses with increasing Gd content, which is due to a change in the deformation mechanism. The results showing that approximately 1.0 wt.% Mn in Mg-Gd systems reduces the degradation rate could be confirmed, which can be explained by a better passivation, even with increased Fe content. The results suggest that the binary Mg-Gd system can be produced more efficiently and with more robust properties by adding Mn. The Mg-Gd system is seen as an example system of other REE-elements in Mg alloys. It can therefore be assumed that the conclusion also allows good transferability to other Mg-REE systems and thermomechanical manufacturing processes.

**Author Contributions:** Conceptualization, B.W., J.H. and J.B.; methodology, J.H., B.W. and J.B.; validation, J.H.; formal analysis, J.H. and B.W.; investigation, J.H.; writing—original draft preparation, B.W. and J.H.; writing—review and editing, B.W., J.B. and R.W.-R.; visualization, B.W. and J.H.; supervision, B.W. and R.W.-R. All authors have read and agreed to the published version of the manuscript.

**Funding:** This research received no external funding.

**Institutional Review Board Statement:** Not applicable.

**Informed Consent Statement:** Not applicable.

**Data Availability Statement:** Due to the size, the different and partly manufacturer-linked file formats, all data are only available on request from the respective authors.

**Acknowledgments:** The authors appreciate the help of Günter Meister during casting experiments with the alloys of this study and Alexander Reichart for his technical support. The authors would like to thank Julia Bode and Carla Vogt from the Technische Universität Bergakademie Freiberg for the chemical analysis of the Gd and Mn content.

**Conflicts of Interest:** The authors declare no conflict of interest.

## References

1. Kammer, C. *Magnesium Taschenbuch 2. Auflage*; Aluminium-Zentrale e.V., Düsseldorf; Alu Media: Düsseldorf, Germany, 2000.
2. Stanford, N.; Atwell, D.; Barnett, M.R. The effect of Gd on the recrystallisation, texture and deformation behaviour of magnesium-based alloys. *Acta Mater.* **2010**, *58*, 6773–6783. [[CrossRef](#)]
3. Stanford, N. The effect of rare earth elements on the behaviour of magnesium-based alloys: Part 2—Recrystallisation and texture development. *Mater. Sci. Eng. A* **2013**, *565*, 469–475. [[CrossRef](#)]
4. Stanford, N. Micro-alloying Mg with Y, Ce, Gd and La for texture modification—A comparative study. *Mater. Sci. Eng. A* **2010**, *527*, 2669–2677. [[CrossRef](#)]
5. Stanford, N.; Barnett, M.R. The origin of “rare earth” texture development in extruded Mg-based alloys and its effect on tensile ductility. *Mater. Sci. Eng. A* **2008**, *496*, 399–408. [[CrossRef](#)]
6. Bohlen, J.; Meyer, S.; Wiese, B.; Luthringer-Feyerabend, B.J.C.; Willumeit-Römer, R.; Letzig, D. Alloying and processing effects on the microstructure, mechanical properties, and degradation behavior of extruded magnesium alloys containing calcium, cerium, or silver. *Materials* **2020**, *13*, 391. [[CrossRef](#)]
7. Bohlen, J.; Yi, S.; Letzig, D.; Kainer, K.U. Effect of rare earth elements on the microstructure and texture development in magnesium-manganese alloys during extrusion. *Mater. Sci. Eng. A* **2010**, *527*, 7092–7098. [[CrossRef](#)]
8. Harmuth, J.; Wiese, B.; Bohlen, J.; Ebel, T.; Willumeit-Römer, R. Tailoring of Material Properties of Mg–Gd Alloys for Biomedical Applications. In Proceedings of the 11th International Conference on Magnesium Alloys and Their Applications, Old Windsor, UK, 24–27 July 2018; pp. 376–381.
9. Huang, Y.; Gan, W.; Kainer, K.U.; Hort, N. Role of multi-microalloying by rare earth elements in ductilization of magnesium alloys. *J. Magnes. Alloy.* **2014**, *2*, 1–7. [[CrossRef](#)]
10. Feyerabend, F.; Fischer, J.; Holtz, J.; Witte, F.; Willumeit, R.; Drücker, H.; Vogt, C.; Hort, N. Evaluation of short-term effects of rare earth and other elements used in magnesium alloys on primary cells and cell lines. *Acta Biomater.* **2010**, *6*, 1834–1842. [[CrossRef](#)]
11. Zeller-Plumhoff, B.; Malich, C.; Krüger, D.; Campbell, G.; Wiese, B.; Galli, S.; Wennerberg, A.; Willumeit-Römer, R.; Wieland, D.C.F. Analysis of the bone ultrastructure around biodegradable Mg–xGd implants using small angle X-ray scattering and X-ray diffraction. *Acta Biomater.* **2020**, *101*, 637–645. [[CrossRef](#)]
12. Moosmann, J.; Zeller-Plumhoff, B.; Wieland, D.C.F.; Galli, S.; Krüger, D.; Dose, T.; Burmester, H.; Wilde, F.; Bech, M.; Peruzzi, N.; et al. Biodegradable Magnesium-Based Implants in Bone Studied by Synchrotron Radiation Microtomography. In Proceedings of the SPIE—The International Society for Optical Engineering, San Diego, CA, USA, 8–10 August 2017.
13. Willumeit-Römer, R.; Moosmann, J.; Zeller-Plumhoff, B.; Florian Wieland, D.C.; Krüger, D.; Wiese, B.; Wennerberg, A.; Peruzzi, N.; Galli, S.; Beckmann, F.; et al. Visualization of implant failure by synchrotron tomography. In *Minerals, Metals and Materials Series*; Springer: Cham, Switzerland, 2018; Volume Part F12, pp. 275–284.
14. Peruzzi, N.; Galli, S.; Helmholz, H.; Kardjilov, N.; Krüger, D.; Markötter, H.; Moosmann, J.; Orlov, D.; Prgomet, Z.; Willumeit-Römer, R.; et al. Multimodal ex vivo methods reveal that Gd-rich corrosion byproducts remain at the implant site of biodegradable Mg–Gd screws. *Acta Biomater.* **2021**, *136*, 582–591. [[CrossRef](#)]
15. Sun, Y.; Helmholz, H.; Will, O.; Damm, T.; Wiese, B.; Luczak, M.; Peschke, E.; Luthringer-Feyerabend, B.; Ebel, T.; Hövener, J.-B.; et al. Dynamic in vivo monitoring of fracture healing process in response to magnesium implant with multimodal imaging: Pilot longitudinal study in a rat external fixation model. *Biomater. Sci.* **2022**, *10*, 1532–1543. [[CrossRef](#)] [[PubMed](#)]
16. Nagarajan, D.; Cáceres, C.H.; Griffiths, J.R. Grain Size Hardening Effects in Mg–Gd Solid Solutions. *Metall. Mater. Trans. A* **2016**, *47*, 5401–5408. [[CrossRef](#)]
17. Xu, Y.; Ren, Z.; Huang, Y.; Kainer, K.; Hort, N. Solid solution strengthening in Mg–Gd alloys. In *Magnesium Technology 2016*; Springer: Cham, Switzerland, 2016; pp. 135–139.
18. Pan, F.; Chen, X.; Yan, T.; Liu, T.; Mao, J.; Luo, W.; Wang, Q.; Peng, J.; Tang, A.; Jiang, B. A novel approach to melt purification of magnesium alloys. *J. Magnes. Alloy.* **2016**, *4*, 8–14. [[CrossRef](#)]

19. Lu, Y.; Huang, Y.; Feyerabend, F.; Willumeit-Römer, R.; Kainer, K.U.; Hort, N. Microstructure and mechanical properties of Mg–Gd alloys as biodegradable implant materials. In *Minerals, Metals and Materials Series*; Springer: Cham, Switzerland, 2018; Volume Part F12, pp. 253–262.
20. Harmuth, J.; Wiese, B.; Bohlen, J.; Ebel, T.; Willumeit-Römer, R. Wide Range Mechanical Customization of Mg–Gd Alloys with Low Degradation Rates by Extrusion. *Front. Mater.* **2019**, *6*, 201. [[CrossRef](#)]
21. Hort, N.; Huang, Y.; Fechner, D.; Störmer, M.; Blawert, C.; Witte, F.; Vogt, C.; Drücker, H.; Willumeit, R.; Kainer, K.U.; et al. Magnesium alloys as implant materials—Principles of property design for Mg–RE alloys. *Acta Biomater.* **2010**, *6*, 1714–1725. [[CrossRef](#)]
22. Krüger, D.; Zeller-Plumhoff, B.; Wiese, B.; Yi, S.; Zuber, M.; Wieland, D.C.F.; Moosmann, J.; Willumeit-Römer, R. Assessing the microstructure and in vitro degradation behavior of Mg-xGd screw implants using  $\mu$ CT. *J. Magnes. Alloy.* **2021**, *9*, 2207–2222. [[CrossRef](#)]
23. Gandel, D.S.; Birbilis, N.; Easton, M.A.; Gibson, M.A. The influence of Mn on the corrosion of Al-free Mg-alloys. In Proceedings of the 18th International Corrosion Congress 2011, Perth, Australia, 20–24 November 2011; pp. 1009–1017.
24. Gandel, D.S.; Easton, M.A.; Gibson, M.A.; Birbilis, N. CALPHAD simulation of the Mg-(Mn, Zr)-Fe system and experimental comparison with as-cast alloy microstructures as relevant to impurity driven corrosion of Mg-alloys. *Mater. Chem. Phys.* **2014**, *143*, 1082–1091. [[CrossRef](#)]
25. Yang, Y.; Wu, P.; Wang, Q.; Wu, H.; Liu, Y.; Deng, Y.; Zhou, Y.; Shuai, C. The Enhancement of Mg Corrosion Resistance by Alloying Mn and Laser-Melting. *Materials* **2016**, *9*, 216. [[CrossRef](#)]
26. Friedrich, H.E.; Mordike, B.L. *Magnesium Technology: Metallurgy, Design Data, Applications*; Springer: Berlin/Heidelberg, Germany, 2006; pp. 1–677.
27. Zeng, G.; Xian, J.W.; Gourlay, C.M. Nucleation and growth crystallography of Al8Mn5 on B2-Al(Mn,Fe) in AZ91 magnesium alloys. *Acta Mater.* **2018**, *153*, 364–376. [[CrossRef](#)]
28. Silva Campos, M.R.; Scharnagl, N.; Blawert, C.; Kainer, K.U. Improving corrosion resistance of Mg10Gd alloy. In *Materials Science Forum*; Trans Tech Publications Ltd.: Bäch, Switzerland, 2013; Volume 765, pp. 673–677.
29. Fang, X.Y.; Yi, D.Q.; Nie, J.F.; Zhang, X.J.; Wang, B.; Xiao, L.R. Effect of Zr, Mn and Sc additions on the grain size of Mg–Gd alloy. *J. Alloy. Compd.* **2009**, *470*, 311–316. [[CrossRef](#)]
30. Wang, J.; Lu, R.; Qin, D.; Huang, X.; Pan, F. A study of the ultrahigh damping capacities in Mg–Mn alloys. *Mater. Sci. Eng. A* **2013**, *560*, 667–671. [[CrossRef](#)]
31. Robson, J.D.; Henry, D.T.; Davis, B. Particle effects on recrystallization in magnesium-manganese alloys: Particle pinning. *Mater. Sci. Eng. A* **2011**, *528*, 4239–4247. [[CrossRef](#)]
32. Yu, Z.; Tang, A.; Wang, Q.; Gao, Z.; He, J.; She, J.; Song, K.; Pan, F. High strength and superior ductility of an ultra-fine grained magnesium-manganese alloy. *Mater. Sci. Eng. A* **2015**, *648*, 202–207. [[CrossRef](#)]
33. Aschner, J.L.; Aschner, M. Nutritional aspects of manganese homeostasis. *Mol. Asp. Med.* **2005**, *26*, 353–362. [[CrossRef](#)] [[PubMed](#)]
34. Gahl, A. Kupfer, Mangan, Chrom, Molybdän—Schätzwerte Für Eine Angemessene Zufuhr. Available online: <https://www.dge.de/wissenschaft/referenzwerte/kupfer-mangan-chrom-molybdaen/> (accessed on 26 March 2022).
35. Trumbo, P.; Yates, A.A.; Schlicker, S.; Poos, M. Dietary reference intakes: Vitamin A, vitamin K, arsenic, boron, chromium, copper, iodine, iron, manganese, molybdenum, nickel, silicon, vanadium, and zinc. *J. Am. Diet. Assoc.* **2001**, *101*, 294–301. [[CrossRef](#)]
36. Dermience, M.; Lognay, G.; Mathieu, F.; Goyens, P. Effects of thirty elements on bone metabolism. *J. Trace Elem. Med. Biol.* **2015**, *32*, 86–106. [[CrossRef](#)]
37. Bachmann, F.; Hielscher, R.; Schaeben, H. Texture analysis with MTEX—Free and open source software toolbox. In *Solid State Phenomena*; Trans Tech Publications: Bäch, Switzerland, 2010; Volume 160, pp. 63–68.
38. Wiese, B.; Willumeit-Römer, R.; Letzig, D.; Bohlen, J. Alloying effect of silver in magnesium on the development of microstructure and mechanical properties by indirect extrusion. *J. Magnes. Alloy.* **2021**, *9*, 112–122. [[CrossRef](#)]
39. Bauser, M.; Sauer, G.; Siegert, K. *Extrusion*; ASM international: Amir, The Netherlands, 2006; Volume 2.
40. Peng, P.; Tang, A.; She, J.; Zhang, J.; Zhou, S.; Song, K.; Pan, F. Significant improvement in yield stress of Mg–Gd–Mn alloy by forming bimodal grain structure. *Mater. Sci. Eng. A* **2021**, *803*, 140569. [[CrossRef](#)]
41. Robson, J.D. Effect of rare-earth additions on the texture of wrought magnesium alloys: The role of grain boundary segregation. *Metall. Mater. Trans. A* **2014**, *45*, 3205–3212. [[CrossRef](#)]
42. Zhu, S.M.; Nie, J.F.; Gibson, M.A.; Easton, M.A. On the unexpected formation of rare earth hydrides in magnesium-rare earth casting alloys. *Scr. Mater.* **2014**, *77*, 21–24. [[CrossRef](#)]
43. Huang, Y.; Yang, L.; You, S.; Gan, W.; Kainer, K.U.; Hort, N. Unexpected formation of hydrides in heavy rare earth containing magnesium alloys. *J. Magnes. Alloy.* **2016**, *4*, 173–180. [[CrossRef](#)]
44. Peng, Q.; Huang, Y.; Meng, J.; Li, Y.; Kainer, K.U. Strain induced GdH<sub>2</sub> precipitate in Mg–Gd based alloys. *Intermetallics* **2011**, *19*, 382–389. [[CrossRef](#)]
45. Vlček, M.; Čížek, J.; Lukáč, F.; Hruška, P.; Smola, B.; Stulíková, I.; Kudrnová, H.; Minárik, P.; Kmječ, T.; Vlasák, T. Hydrogen absorption in Mg–Gd alloy. *Int. J. Hydrogen Energy* **2017**, *42*, 22598–22604. [[CrossRef](#)]
46. Grey, E.A.; Higgins, G.T. Solute limited grain boundary migration: A rationalisation of grain growth. *Acta Metall.* **1973**, *21*, 309–321. [[CrossRef](#)]

47. Kim, S.H.; Jung, J.G.; You, B.S.; Park, S.H. Microstructure and texture variation with Gd addition in extruded magnesium. *J. Alloy. Compd.* **2017**, *695*, 344–350. [[CrossRef](#)]
48. Yu, H.; Kim, Y.M.; You, B.S.; Yu, H.S.; Park, S.H. Effects of cerium addition on the microstructure, mechanical properties and hot workability of ZK60 alloy. *Mater. Sci. Eng. A* **2013**, *559*, 798–807. [[CrossRef](#)]
49. Dobroň, P.; Drozdenko, D.; Olejňák, J.; Hegedüs, M.; Horváth, K.; Veselý, J.; Bohlen, J.; Letzig, D. Compressive yield stress improvement using thermomechanical treatment of extruded Mg-Zn-Ca alloy. *Mater. Sci. Eng. A* **2018**, *730*, 401–409. [[CrossRef](#)]